AIAA 81-0332R

Transonic Flow Past Axisymmetric and Nonaxisymmetric Boattail Projectiles

Stephen S. Stahara* and James P. Elliott†
Nielsen Engineering and Research, Inc., Mountain View, California
and
John R. Spreiter‡
Stanford University, Stanford, California

The development of a predictive method for investigating the steady inviscid aerodynamic behavior of ballistic projectiles having various axisymmetric and nonaxisymmetric boattail shapes is reported. These shapes include the now standard conical boattail as well as a variety of nonaxisymmetric shapes. The theoretical procedure employs the classical transonic equivalence rule and a new transonically corrected apparent mass loading method. Theoretical results for surface pressures, loadings, and static aerodynamic characteristics are presented throughout the transonic range for a variety of projectiles having different boattail geometries. Comparisons with results of both experiment and other theoretical methods demonstrate the accuracy of the procedure.

Introduction

TYPICAL projectiles in current use by the Army are slender, spin-stabilized bodies of revolution. The boattail configuration that has become the standard is a conical shape with a relatively shallow cone angle $\sim(5-10$ deg). The primary purpose of any boattail is to increase the projectile range by reducing drag from what it would be if the projectile afterbody were cylindrical. While drag reduction is accomplished, an associated detrimental result is the creation of negative lift on the boattail. This tends to increase further the destabilizing pitching moment produced by positive lift on the nose, and thereby to reduce additionally the gyroscopic stability of the projectile. At transonic flight speeds, which usually occur near ballistic trajectory apex, the negative loading on the boattail is strongly augmented by the development and movement of shock waves on the boattail. This results in a rapid peaking of the destabilizing pitching moment at flight Mach numbers just below one. That and related changes of other aerodynamic characteristics can result in the projectile becoming unstable.

In an effort to reduce the adverse transonic behavior of ballistic projectiles, the Army has recently investigated experimentally[1] a series of nonaxisymmetric boattail shapes. Some of these were found to improve significantly the aerodynamic characteristics over those of the conical configuration. In particular, it was found that increased gyroscopic and dynamic stability and decreased drag could be attained simultaneously. These findings are of considerable importance because they showed for the first time that projectiles designed with such shapes would have both increased range and improved stability compared with projectiles employing the standard boattail.

The present work describes the development of a theoretical method for predicting the transonic static aerodynamic characteristics of these projectiles. The theoretical analysis for determining the nonlinear three-dimensional projectile flowfields is based on the classical transonic equivalence rule (TER). A new loading calculation method based on apparent mass concepts and which makes use of nonlinear TER flow solutions is used to predict the static aerodynamic coefficients. Theoretical results for surface pressures, loadings, and static aerodynamic coefficients are presented for a variety of projectiles with different boattail geometries at Mach numbers throughout the transonic range. Comparisons are made insofar as possible with both other theoretical methods and experimental results.

Analysis

General

The most notable feature of transonic flow past ballistic projectiles is the formation and movement as a function of freestream Mach number of a variety of shock waves in the flowfield surrounding these configurations. This is clearly evident in shadowgraphs, such as shown in Fig. 1, which illustrate the phenomena for selected Mach numbers near unity.

The result of shock formations and their rapid movement on projectile aerodynamic characteristics is a sharp peaking near $M_\infty = 1$. As illustrated in the sketches in Fig. 2, both the overturning pitching moment and drag coefficients strongly exhibit this behavior. With regard to the overturning pitching moment, the sketch in Fig. 2 displaying a simplified projectile shock pattern illustrates why this occurs. At angle of attack, the shock positions on the windward surface are displaced farther aft than on the leeward side, resulting in a strong negative loading at those axial locations. Both shock strength and negative loading are strongest by a considerable amount for the boattail shock. As the Mach number increases and the boattail shock moves further aft, the strength of the negative loading and its moment arm from the center of mass of the projectile increase, and result in a peak pitching moment occurring just prior to the shock moving off the boattail. This inevitably happens at a Mach number just below one. As the Mach number increases beyond that value, the destabilizing pitching moment decreases rapidly and usually smoothly, and then eventually plateaus as the Mach number increases further supersonically.

Transonic Equivalence Rule

The basic equations and boundary conditions governing the classical or thickness-dominated transonic equivalence rule formulation have been presented in Ref. 2. Here we provide

Presented as Paper 81-0332 at the AIAA 19th Aerospace Sciences Meeting, St. Louis, Mo., Jan. 12-15, 1981; submitted Feb. 10, 1981; revision received Feb. 5, 1982.

*Department Manager, Theoretical Fluid Mechanics. Associate Fellow AIAA.

†Research Scientist; currently with Compression Labs, Inc., San Jose, Calif.

‡Professor, Division of Applied Mechanics; consultant Nielsen Engineering and Research, Inc. Fellow AIAA.

only a brief summary to cover several salient points important to the present application.

The theoretical essentials of the classical TER are illustrated in Fig. 3, which displays the decomposition of the flow into its first-order inner and outer components and the resulting uniformly valid composite perturbation solution,

$$\phi = \phi_{2,\alpha} + \phi_{2,t} + \phi_{2,\omega} - \phi_{2,B} + \phi_B \tag{1}$$

For the low to moderate lift situations for which this form applies, the TER solution domains consist of an inner region governed by a linear equation, the same as in slender body theory, and an outer nonlinear region consisting of the axisymmetric flow about an "equivalent" nonlifting body of revolution having the same longitudinal distribution of cross-sectional area. Each component of the composite solution has the meaning indicated in Fig. 3. The first-order lift $\phi_{2,\alpha}$, thickness $\phi_{2,t}$, and rotation $\phi_{2,\omega}$ inner solution components describe, respectively, the translating, expanding, and rotating cross section in the y,z plane, and satisfy the two-dimensional Laplace equation shown in the figure together with the zero normal flow boundary condition at the body. The first-order outer solution ϕ_B satisfies the axisymmetric transonic small-disturbance equation subject to an inner boundary condition determined by the equivalent body singularity source distribution which, in turn, is determined by the outer behavior of the inner solution. Details of the outer flow solution computational procedure used are provided in Ref. 3 where extensive comparisons with data are reported for a variety of body shapes throughout the transonic regime, and demonstrate the accuracy of the procedure. The computational procedure developed to determine the inner flow solutions is discussed in the following section.

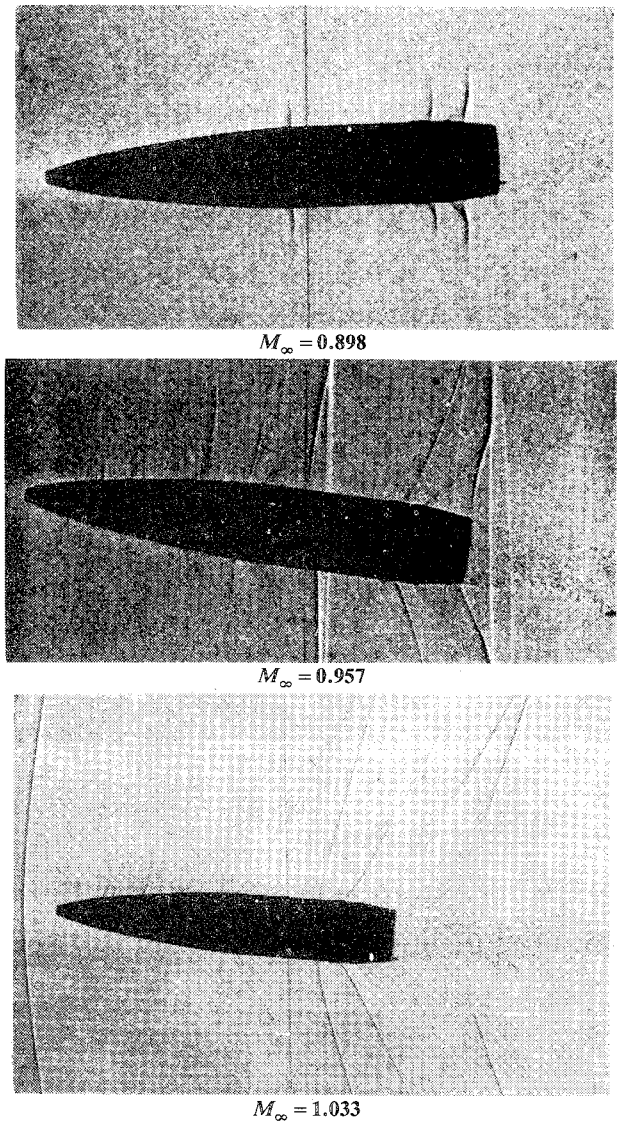

Fig. 1 Shadowgraphs of ballistic projectiles at various transonic Mach numbers illustrating characteristic shock formation and movement.

Inner Flow Solution

The determination of the inner flow problem consists of solving the cross-flow Laplace equation for the three components, $\phi_{2,\alpha}$, $\phi_{2,t}$, and $\phi_{2,\omega}$. The component $\phi_{2,B}$, in Eq. (1) represents the outer behavior of the inner solution, and for the thickness-dominated flows considered here is given analytically by

$$\phi_{2,B} = \frac{S'(x)}{2\pi} \ln r \tag{2}$$

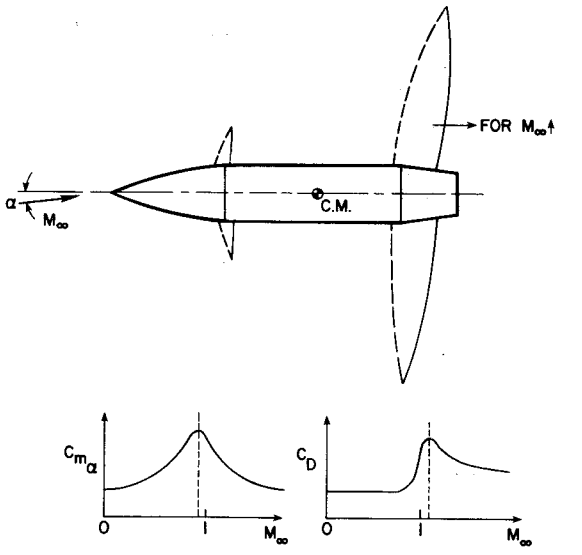

Fig. 2 Variation of the shock movement, destabilizing pitching moment, and drag with M_∞ on a typical ballistic projectile.

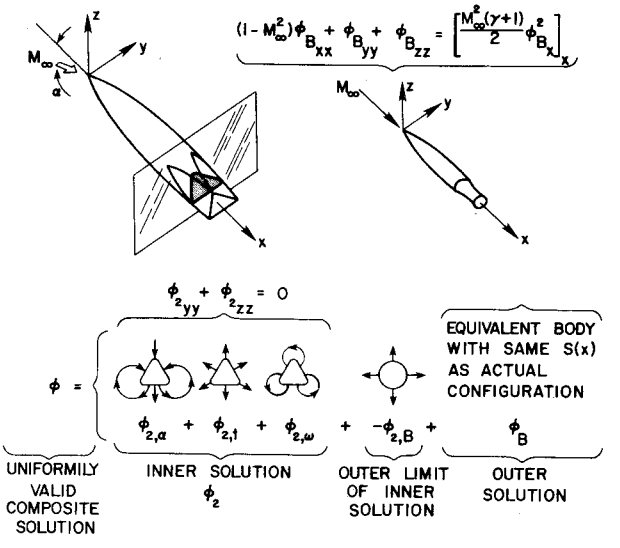

Fig. 3 Illustration of the classical transonic equivalence rule for slender configurations.

For the axisymmetric portion of the projectile, the three inner solutions can be determined analytically, and are

$$\phi_{2,\alpha} = \frac{\alpha S(x)}{\pi} \frac{\sin\theta}{r} \tag{3}$$

$$\phi_{2,t} = \frac{S'(x)}{2\pi} \ell n\, r \tag{4}$$

$$\phi_{2,\omega} = 0 \tag{5}$$

Along the nonaxisymmetric boattail, general analytic expressions cannot be given for the typical cross-sectional shapes of interest to this study. Those shapes comprise a general class of contours formed by N ($N \geq 3$) equal-length, flat-sided segments separated by N equal-angle circular arc segments, and are formed by cutting planes acting on the axisymmetric projectile boattail. Those cutting planes are inclined at a small angle to the main projectile axis, and result in flat surfaces being formed longitudinally on the boattail. In general, these cutting planes are rotated about the projectile axis as they proceed downstream so as to provide twist to the cut surface and thereby prevent projectile despinning. Figure 4 provides an illustration of two such boattail shapes formed by three and four cutting planes. For those shapes, the basic axisymmetric boattail was cylindrical rather than conical, the cutting planes were not rotated, and the cutting plane angles and axial starting locations were chosen such that the cutting planes meet at the boattail end and result in an inscribed triangle and square, respectively.

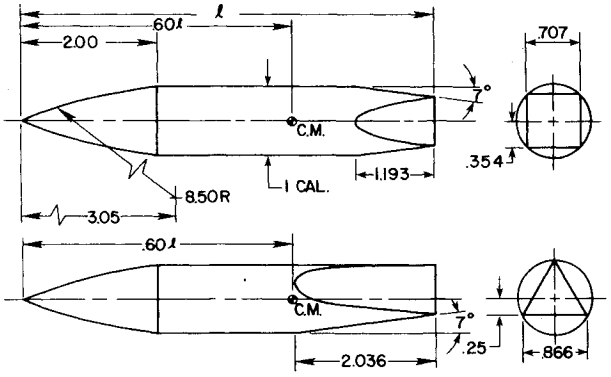

Fig. 4 Ballistic projectiles having inscribed square and triangular boattail shapes formed by cutting planes acting on the cylindrical boattail section.

The computational method employed to determine the inner flow solutions is a finite element procedure. The procedure uses the Galerkin method of weighted residuals and employs isoparametric quadrilateral elements with quadratic shape functions of the serendipity type. The linear, symmetric matrix equations that result from discretization of the Laplace equation are solved directly using Gaussian elimination. The body surface boundary conditions for each of the three inner computational problems are summarized in Fig. 5. In the computational procedure they are implemented via a Neumann flux condition. On the outer boundary of the finite element mesh, Neumann conditions are also employed for each of the component problems as this was found to be both much more convenient and of essentially equal accuracy compared with using the corresponding Dirichlet conditions. A typical finite element mesh employed is illustrated in Fig. 6. That figure displays the mesh for a body formed by three cutting planes acting on a circular cross section such that a sectored triangular shape results in which the circular arc segments subtend 30-deg angles. The mesh shown consists of 6 rings extending radially outward from the body surface and having 12 quadrilateral elements per ring. The radial spacing of the rings is geometrical, and for the mesh illustrated here the geometric spacing ratio r_i/r_{i-1} was 1.4.

A series of numerical experiments were performed in order to examine inner solution accuracy as a function of mesh parameters, viz. number of rings, number of elements per ring, radial mesh spacing ratio, and outer boundary location. The results indicated that mesh configurations similar to that shown in Fig. 6 were adequate with regard to both number of rings and elements per ring, provided that the outer boundary was located approximately at 8 body radii and that the mesh radial spacing near the body surface was slightly more compact than shown in the figure. A geometric spacing ratio of 2.0 was found to be satisfactory.

Figure 7 provides an indication of the typical accuracy of the finite element solver when applied to one of the three component problems. Displayed are the surface velocity components for the contraction problem for the 30-deg sectored triangular cross section shown in Fig. 6. The predicted velocities shown have been adjusted so as to be relative to the local body surface, and thus should be precisely tangential to the local surface. The particular contraction problem solved was for a unit contraction of the flat segments ($\phi_n = dF/dx = -1$) and stationary circular arc segments

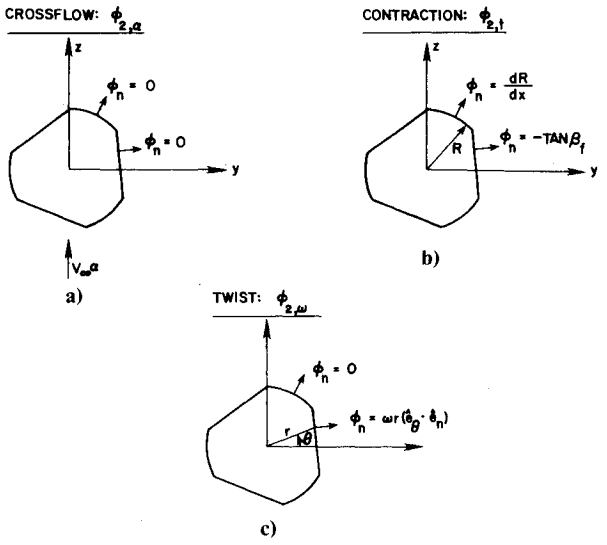

Fig. 5 Body surface boundary conditions for inner flow computational problem.

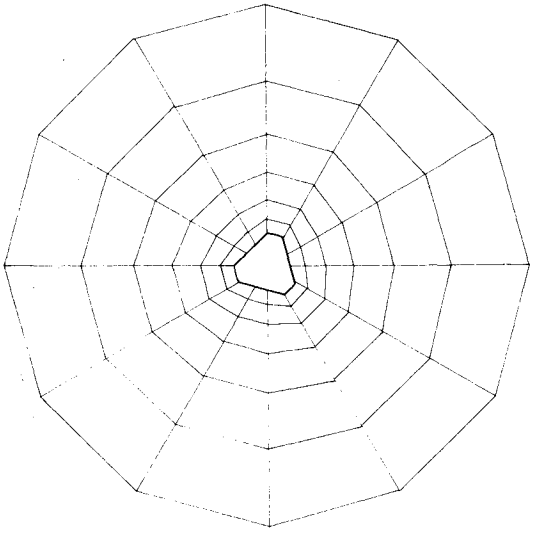

Fig. 6 Illustration of typical finite element mesh employed for inner problem.

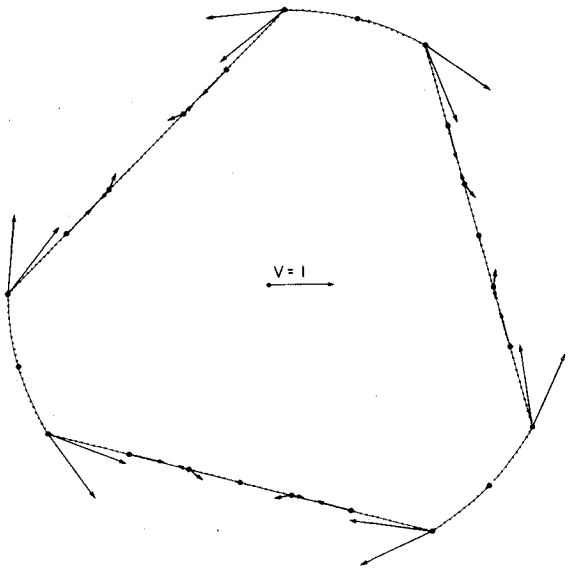

Fig. 7 Body surface cross-flow velocities predicted by finite element solver for a typical contraction inner problem, viewed relative to local surface.

($\phi_n = dR/dx = 0$). The surface velocity vectors on both the flat and circular segments are, indeed, essentially tangential to the local surface. At the junctions of the flat and circular segments, two vectors are indicated since for those points a velocity vector can be predicted employing values of the potential associated either with the element lying on the circular segment or the adjacent element lying on the flat segment. Potential theory is, in fact, discontinuous at those locations; and although velocities exactly at those corner points are never used or required in any of the calculations performed here, it is, nevertheless, instructive to observe the behavior of the finite element solver at those singular points. As is evident from the result shown in Fig. 7, the solver provides both the correct trend (high magnitude) and direction (tangential to the surface) of the solution behavior at those locations.

Loading Calculation

The objective of the development and application of the TER procedure to ballistic projectiles was to provide a means for determining the transonic flowfields about these shapes and, subsequently, the surface pressures and resultant steady aerodynamic forces and moments. However, the primary quantities of concern are the static aerodynamic characteristics. Consequently, the calculation and integration of surface pressures predicted via the TER method over the entire projectile is an undesirable intermediate and computationally expensive step. Consistent with the order of accuracy of the present flow solution, it is possible to formulate a procedure based on the TER method and slender body theory which avoids that step and provides the axial loading distribution directly.

This procedure, known as the method of apparent masses,[4] relates the kinetic energy of the fluid per unit axial length to contour integrals involving various cross-flow velocity potentials describing the translation, rotation, etc. of the cross section. These contour integrals are relatable to the apparent mass coefficients of the configuration cross section, and with those coefficients in hand, the determination of the lateral force and moment distributions is direct.

The utility of the apparent mass method is in the determination of stability derivatives, both static and dynamic. The method has been employed successfully in the past in a wide number of aerodynamic applications,[5] particularly for missile configurations. A detailed formulation of the method for combined upwash, sidewash, and roll providing all the important static and dynamic stability derivatives is provided in Ref. 5. The previous applications of the method have focused exclusively in the subsonic and supersonic regimes where the governing small-disturbance potential equations are linear. Since slender body theory is valid equally throughout the transonic regime and, in fact, underlies the basis of the TER, application of the apparent mass method at transonic speeds is feasible. However, a well-known result of the classical TER method,[6,7] and verified by experiment for certain classes of aerodynamic configurations,[6] is that the loading distributions and thus the lateral forces and moments are independent of freestream Mach number. This, of course, is not the case for typical projectiles, as noted in Fig. 2. The reason for this discrepancy lies not in an overall breakdown of the TER theory, but rather in the failure to take into account locally the large axial gradients which occur in the vicinity of shock waves located on the body surface. These large gradients locally violate the moderate axial gradient hypothesis inherent in the apparent mass method.

Because the deficiency of the procedure for applications at transonic speeds is associated primarily with the behavior of the axial velocity component in the vicinity of shock waves, we have postulated and successfully tested the following modification of the classical apparent mass method: 1) correct the axial velocity in the classical apparent mass formulation by replacing the freestream velocity by the local axial velocity, and 2) apply a similar correction to the lateral velocities since they are normalized by the axial velocity component. Here, the local perturbation axial velocity component to be added to the freestream velocity is provided by the TER composite solution Eq. (1). However, since the effect we are attempting to correct for is a transonic one, and since the two-dimensional cross flow solutions contained in Eq. (1) are independent of M_∞, it is sufficient to consider the local axial velocity as augmented by the equivalent body perturbation component alone, viz.

$$V_x = 1 + \phi_{B_x} \tag{6}$$

In order to implement these ideas, consider the normal force loading distribution dC_N/dx for combined angle of attack α, sideslip β, and roll rate ω of a typical ballistic projectile. Although we have not considered sideslip in our derivations of the TER method, it would be a straightforward extension to do so. The transonically corrected classical loading distribution is then given by

$$\frac{dC_N}{dx} = 2\left[V_x \frac{\partial}{\partial x}(M_{12}v_1 + M_{22}v_2 + M_{23}\omega) - \omega(M_{11}v_1 + M_{12}v_2 + M_{13}\omega)\right] \tag{7}$$

where

$$M_{ij} = -\oint_c \phi_i \frac{\partial \phi_j}{\partial n} ds \tag{8}$$

$$V_x = 1 + \phi_{B_x} \tag{9}$$

$$v_1 = \beta(1 + \phi_{B_x}) \tag{10}$$

$$v_2 = \alpha(1 + \phi_{B_x}) \tag{11}$$

Here, the M_{ij} are apparent mass coefficients determined from the following inner flow solution representation (see Fig. 3).

$$\phi_2 = \phi_{2,\beta} + \phi_{2,\alpha} + \phi_{2,\omega} + \phi_{2,t} = \beta\bar{\phi}_1 + \alpha\bar{\phi}_2 + \omega\bar{\phi}_3 + \phi_{2,t} \tag{12}$$

where $\bar{\phi}_1$, $\bar{\phi}_2$, $\bar{\phi}_3$ represent cross-flow potentials for unit horizontal and vertical translation and unit angular rotation,

respectively, of the cross section; v_1, v_2 the transonically corrected sidewash and upwash; and the normal force coefficient is defined by

$$C_N = Z/(\tfrac{1}{2}\rho_\infty V_\infty^2 \pi R_{\max}^2) \tag{13}$$

where Z is the normal force, (ρ_∞, V_∞) the freestream density and velocity, and $R_{\max}$ the projectile maximum radius. Thus, for a projectile having a conical boattail for which the apparent mass coefficients are known analytically ($M_{11}=M_{22}=\pi R^2$, $M_{12}=M_{23}=M_{13}=0$), at zero sidewash and roll rate ($\beta=\omega=0$), the normal force loading distribution is given by

$$\frac{dC_N}{dx} = 2\alpha(1+\phi_{B_x})\frac{d}{dx}\left[(1+\phi_{B_x})\left(\frac{R(x)}{R_{\max}}\right)^2\right] \tag{14}$$

The static normal force and overturning pitching moment coefficients $C_{N\alpha}$, $C_{m\alpha}$ can then be determined from

$$C_{N_\alpha} = \frac{\partial}{\partial\alpha}\int_0^l \frac{dC_N}{dx}dx \tag{15}$$

$$C_{m_\alpha} = \frac{\partial}{\partial\alpha}\int_0^l (x_{c_m}-x)\frac{dC_N}{dx}dx \tag{16}$$

where x_{c_m} is the overturning moment center and the pitching moment is defined as positive nose-up.

While the classical apparent mass method fails to provide the correct loading distribution in regions of high axial gradients, the question of how the TER correction given in Eqs. (9-11) locally effects the loading in the vicinity of the shock is of primary interest. The issue is how this correction together with thickness-dominated TER solutions that contain only axisymmetric shock waves can replicate the actual three-dimensional lifting flow about a projectile in the vicinity of the shock. In this regard, two important physical phenomena are necessary to simulate accurately. The first relates to the prediction of the location and movement with changing freestream Mach number of the shocks on the projectile. The second relates to the observation that the shock positions on projectiles at angle of attack are differentially displaced such that those on the windward surface are farther aft than on the leeward surface. At the low to moderate angles of attack necessary for stable projectile flight, shock location and movement with Mach number is accurately predicted in a mean sense by the axisymmetric shock location. This fact can be verified analytically by comparison of three-dimensional shock patterns past lifting bodies with the corresponding axisymmetric patterns,[8] and can also be anticipated physically since, unlike two-dimensional flow, the perturbation of moderate lift on slender body shock patterns is confined locally near the body surface, with the tendency of the flow to return rapidly to axisymmetric.[8] With regard to windward/leeward shock location displacement, it has been observed experimentally from photographs, such as those shown in Fig. 1, that shock patterns formed on projectiles often appear normal to the freestream direction rather than to the projectile axis. This observation suggests a wind invariant shock conjecture, as shown in Fig. 8, in which shocks appearing on the projectile are taken as normal to the oncoming wind. For the classical TER analysis, this would correspond to holding the axisymmetric shock pattern invariant and then tilting the body with respect to the shock by the oncoming angle of attack. This conjecture is consistent with both slender body theory as well as the classical TER formulation illustrated in Fig. 3. In both of those formulations, the analyses are generally initiated in freestream normal planes and then switched to body-normal planes for convenience, with the difference between freestream normal and body-normal planes, after accounting for oncoming velocity direction, regarded as of higher order.

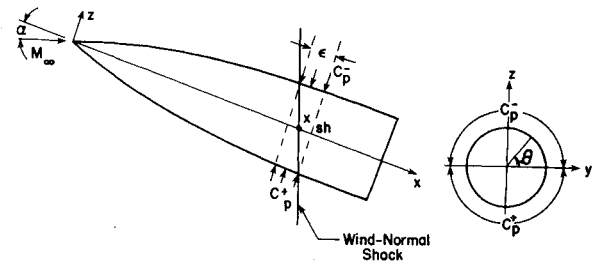

Fig. 8 Interpretation of TER-corrected apparent mass method via a wind invariant shock conjecture.

We will now establish the physical basis of the TER-corrected apparent mass method by demonstrating that the shock-induced impulsive increment in normal force predicted by that method is identical to that given by the wind invariant shock conjecture. Consider a single shock located at $x=x_{\rm sh}$, and designate an axial distance ϵ centered about that location as that which will carry the shock-induced incremental load. The normal force coefficient increment due to the shock for an axisymmetric projectile as given by the TER-corrected apparent mass method is

$$\Delta C_N(x_{\rm sh}) = \int_{x_{\rm sh}-(\epsilon/2)}^{x_{\rm sh}+(\epsilon/2)} \frac{dC_N}{dx}dx \tag{17}$$

where dC_N/dx is given by Eq. (14).

In the neighborhood of $x_{\rm sh}$, the integrand can be approximated as

$$\frac{dC_N}{dx} \simeq 2\alpha\left[\frac{R(x_{\rm sh})}{R_{\max}}\right]^2 \frac{d}{dx}[\phi_{B_x}] \tag{18}$$

since the factor $(1+\phi_{B_x})$ outside the derivative in Eq. (14) is of order $1+0(\tau^2)\simeq 1$ even at the shock, and $R(x)$ is continuous through the shock. Thus,

$$\Delta C_N(x_{\rm sh}) \simeq -2\alpha\left[\frac{R(x_{\rm sh})}{R_{\max}}\right]^2 [\phi_{B_x}^+ - \phi_{B_x}^-] \tag{19}$$

and the normal force increment is

$$\Delta Z(x_{\rm sh}) = -\alpha\pi R^2(x_{\rm sh})\rho_\infty V_\infty^2[\phi_{B_x}^+ - \phi_{B_x}^-] \tag{20}$$

where $(+,-)$ denote preshock and postshock values, respectively.

For the wind invariant shock conjecture we have, with reference to Fig. 8,

$$\Delta Z(x_{\rm sh}) = \int_0^\pi \Delta p\, dA \tag{21}$$

where the differential pressure acting around the cross section at the shock is given by

$$\Delta p = \tfrac{1}{2}\rho_\infty V_\infty^2(C_p^+ - C_p^-) \tag{22}$$

Now the incremental surface areas that the differential pressure acts on can be approximated by

$$dA = R\alpha R\, d\theta \tag{23}$$

and the pressure coefficient via the TER approximation is given by[9]

$$C_p = -2\phi_{B_x} - \left(\frac{dR}{dx}\right)^2 - 4\alpha\left(\frac{dR}{dx}\right)\sin\theta - \alpha^2(-1+\cos^2\theta) \quad (24)$$

Thus, substituting Eqs. (22-24) in Eq. (21), we have

$$\Delta Z(x_{sh}) \doteq -\alpha\pi R^2(x_{sh})\rho_\infty V_\infty^2[\phi_{B_x}^+ - \phi_{B_x}^-] \quad (25)$$

which is the identical result given by Eq. (20).

To summarize, then, the TER-corrected apparent mass loading procedure employs the separate inner and outer flow solution computational procedures as follows. First, the finite element inner flow solver is used to determine the apparent mass coefficients required by Eq. (8), which for the nonaxisymmetric boattail cross sections of interest here cannot be determined analytically. Next, the finite-difference outer flow solver is used to determine the equivalent body solution ϕ_B required in Eqs. (9-11) to correct the slender body axial and lateral velocity components. The normal force loading is then determined from Eq. (7), and the determination of detailed body surface pressures and their subsequent integration over the entire surface is avoided.

Results

To examine the applicability of the transonic equivalence rule for determining transonic flows past ballistic projectiles, as well as to test the validity and accuracy of the proposed nonlinear loading procedure, we have applied these procedures to predict the surface pressures, loading distributions, and static aerodynamic coefficients for a variety of different projectiles at flow conditions throughout the transonic range. In the following sections, we provide some selected results typical of the projectile calculations performed.

Surface Pressures

Insofar as the basic validity and range of accuracy of the TER method for predicting transonic flowfields past slender bodies are concerned, extensive comparisons of TER results with data have been made and are provided in Ref. 2. There, experimental results and TER theory are compared for body surface pressures obtained in conventional transonic tunnels for a number of different axisymmetric and nonaxisymmetric shapes. The configurations include both smooth bodies as well as projectile-like shapes. Those results, which also incorporated wind-tunnel interference effects, provide the most extensive comparison of the classical equivalence rule with experiment. They indicate good agreement with data, including the region near shock waves, at oncoming Mach numbers throughout and beyond the transonic regime for low to moderate angles of attack.

Here, we provide some further results for a specific projectile shape. In Fig. 9 we have exhibited TER results for the surface pressure coefficient on a secant ogive nose, straight cylindrical midbody, and 7-deg conical boattail projectile at $M_\infty = 0.94$ and $\alpha = 4$ deg. These results display the typical axial and azimuthal surface pressure variations characteristic of transonic flows past standard ballistic projectile shapes. The most notable feature of the results is the prominent expansion and compression spikes in the vicinity of the nose/midbody and midbody/boattail junctures. They are associated with the rapid acceleration and deceleration of the flow in those regions where the surface geometry is discontinuous.

The TER results exhibited in Fig. 9 provide the surface pressures along longitudinal rays at the windward, leeward, and midbody azimuthal positions. Also shown are Reklis et al.'s[10] three-dimensional transonic small-disturbance (3-D TSD) results for pressures along the windward ray. The agreement between the two theoretical methods is quite good everywhere, with the only exception being some minor disagreement in the pressure spike regions near the nose/midbody and midbody/boattail junctions. At those locations, the TER results predict a slightly higher and earlier expansion. However, it is probable that even these slight discrepancies are attributable to different grid densities and/or boundary condition treatment in those locations rather than from the difference in the level-of-approximation of the two methods.

Loading Distributions

In order to check and verify the proposed loading calculation method, we have employed the procedure to predict loadings on a number of different projectile shapes for which results from other theoretical methods are available. Figure 10 presents a comparison of results for the normal force distribution on an idealized 5.6-caliber length M549 projectile at $M_\infty = 0.95$ and $\alpha = 1$ deg. For these comparisons, the geometry of the actual projectile shape has been simplified

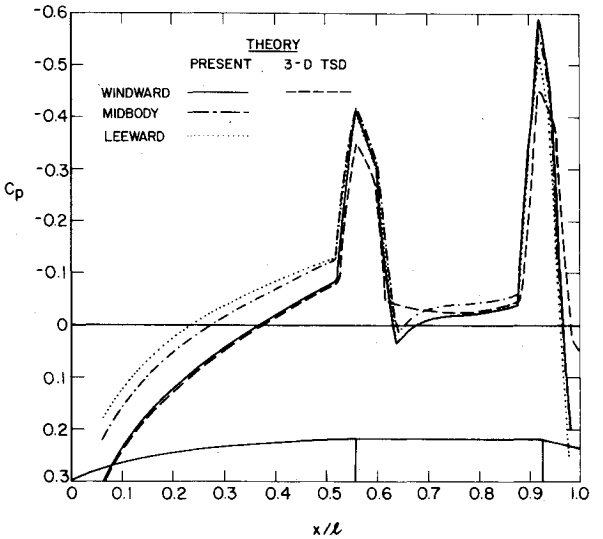

Fig. 9 Prediction of surface pressures on secant ogive/cylinder/7-deg conical boattail projectile at $M_\infty = 0.94$, $\alpha = 4$ deg.

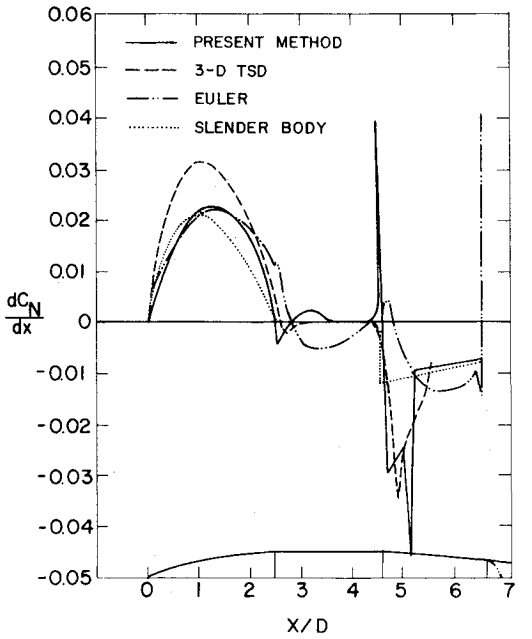

Fig. 10 Comparison of present loading method with other theoretical methods for the normal force loading distribution on an idealized M549 projectile at $M_\infty = 0.95$, $\alpha = 1$ deg.

by considering the nose as sharp, by neglecting the rotating bands, and by simulating the afterbody wake geometry by extending the conical boattail beyond the actual projectile length.

In addition to the present method, results from the 3-D TSD procedure of Reklis et al.,[11] from three-dimensional Euler equation calculations,[8] and from slender body theory are provided in the figure. On the ogive nose, the present method and the Euler equation result compare quite closely and are only moderately removed from the slender body result. However, the 3-D TSD results predict a noticeably higher loading for reasons which are not clear. On the cylindrical midbody, the present method indicates a slight positive loading at points beyond the immediate vicinity of the ogive/midbody juncture; whereas, the Euler results predict a negative loading over the majority of the cylindrical midbody, and the 3-D TSD results show essentially no loading at all. The slender body loading along that unchanging cylindrical cross section is, or course, zero.

As the discontinuity in surface slope at the midbody/boattail juncture is approached and passed, the present method displays first a large positive then negative loading spike corresponding to the rapid flow expansion and compression at that location. Downstream of the junction, the present theory displays another sharp spike, due to the boattail shock. Once beyond the boattail shock, the present method essentially provides the slender body result. Along the boattail, the corresponding 3-D TSD result displays no expansion spikes at the boattail junction. However, similar to the present theory, the result indicates the same strong downward loading spike on the main boattail section due to the boattail shock, although the peak is displaced slightly rearward from the present theory prediction. With regard to the Euler equation prediction on the boattail, a positive loading is indicated just beyond the boattail juncture and then an increasing negative loading on the remainder of the boattail. In the Euler calculation, the boattail was extended to $x/D=6.5$ at which point for numerical convenience a spherical cap as indicated was added to close the body. That spherical cap, which was located sufficiently far downstream so as not to influence the solution on the actual projectile, locally induces a sharp discontinuous behavior which is to be disregarded. At first glance, the Euler result appears to be quite different from the present theory and the 3-D TSD result over the major portion of the boattail. We believe, however, that this is, in fact, not the case since the Euler prediction was carried out on a much coarser computational grid than both the present method and the 3-D TSD calculation. That has resulted in a broad smearing of the boattail shock, and it is felt that increasing the grid density would result in good correspondence between the Euler result and the present method. In particular, we observe that, as in the present result, a positive expansion loading exists in the Euler prediction near the boattail junction. Finally, with regard to the overall agreement evident from these comparisons, we note that the present loading method is able to capture all of the critical features of the loading behavior for this typical projectile geometry as predicted by other more accurate but computationally far more expensive procedures. Consequently, based on these and other related comparisons, we have concluded that the proposed transonically corrected loading method is able to capture the primary nonlinear inviscid transonic effects which exist on typical ballistic projectiles.

Static Aerodynamic Coefficients for Various Boattail Projectiles

The ultimate objective of the development of the TER solution procedure and the transonically modified loading method is in the prediction of the static aerodynamic coefficients of various boattail ballistic projectiles. In Figs. 11-15 we provide results of the application of these procedures to a variety of different projectile shapes at conditions throughout the transonic regime.

Figure 11 exhibits a comparison of results from the present theory with 3-D TSD results and some limited data[11] for the variation of the overturning pitching moment coefficient C_{m_α} with oncoming Mach number M_∞ for an idealized M549 projectile having a 0.579-caliber boattail length. For both theoretical results, the actual nose was replaced by a sharp one of equal length, the rotating bands were neglected so that the cylindrical midbody was smooth, and the afterbody wake geometry was simulated by extending the conical boattail downstream. Both theoretical methods display essentially identical variation with M_∞ and peak C_{m_α} value, but with the 3-D TSD results displaced forward in M_∞ by approximately 0.05. The range data indicate a slightly higher peak value, occurring at the same Mach number predicted by the present method.

To examine the effect of various idealizations of projectile geometry that were made to facilitate some of these initial calculations, we have performed several parametric studies involving the independent variation of selected projectile geometry parameters. These primarily have involved investigating the idealizations of afterbody wake geometry and approximations of nose geometry, although a preliminary investigation of bore rider influence has also been made. Figure 12 provides the effect of a different nose and afterbody wake geometry on the variation of C_{m_α} with M_∞ for the idealized M549 projectile, for which results for the sharp

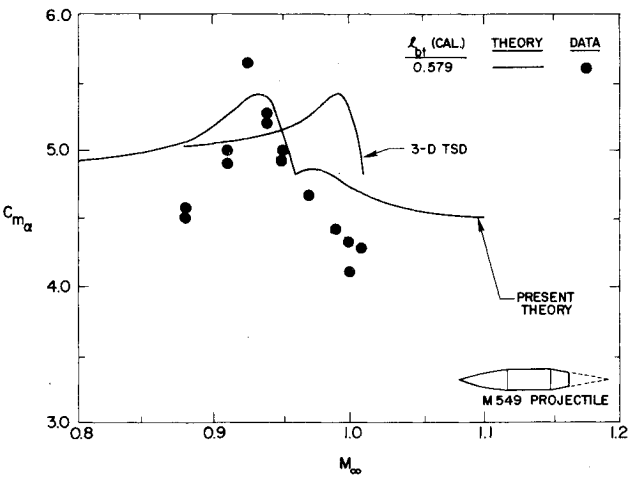

Fig. 11 Comparison of present method with 3-D TSD results and data for the variation of destabilizing pitching moment C_{m_α} with M_∞ for a basic M549 projectile.

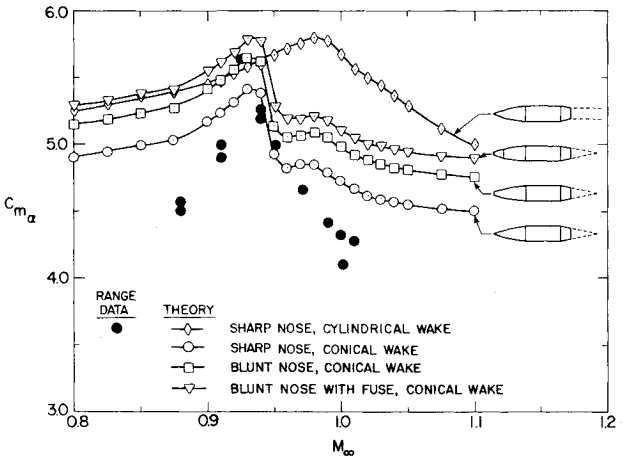

Fig. 12 Effects of afterbody wake geometry and nose bluntness on variation of C_{m_α} with M_∞ for a M549 projectile.

nose, conical wake geometry model were presented previously in Fig. 11. The four theoretical results include the following geometry combinations: 1) sharp nose, cylindrical wake; 2) sharp nose, conical wake; 3) blunt nose, conical wake; and 4) blunt nose with fuze, conical wake. Limited range data[11] are also presented for the actual projectile. We note that the difference between the cylindrical and conical wake model results in the largest change in C_{m_α}, with the continuous conical wake model most certainly being the more accurate simulation of the actual wake flow rather than the discontinuous cylindrical model. The shift in peak C_{m_α} location and the change to a more peaky behavior in the vicinity of the maximum resulting from the change from cylindrical to conical wake model confirms this, and exhibits excellent agreement with the range data. The addition of the blunt nose to the conical wake model projectile results in an upward shift in magnitude C_{m_α} (but no essential difference in trend from the sharp nose result) and continues to bring the theoretical prediction in closer accord with the data near the maximum. The final addition of the fuze geometry to the blunt nose results in a similar but smaller change. The importance of modeling as much as possible of the geometric detail of the actual projectile, however, is clear.

In Fig. 13 we present a similar comparison of theoretical results and range data for C_{m_α} vs M_∞ for a T388 projectile.[12] The standard projectile has a 5.58-caliber overall length, 2.90-caliber ogive nose, and 0.59-caliber conical boattail with 7-deg 35-s boattail angle. Theoretical predictions are presented based on a 1) sharp nose, cylindrical wake; 2) sharp nose, conical wake; and 3) blunt nose, conical wake. As with the M549 projectile, the change from cylindrical to conical wake model brings the predicted results into almost exact agreement with the range data. Addition of the blunt nose in the theoretical calculation for this projectile results in a downward shift in C_{m_α} level, opposite to that of the M549, indicating the interdependence of such geometric changes.

In Fig. 14 we provide the final comparison between the present theory and range data for a standard conical boattail projectile. The figure compares theoretical results with both range and tunnel data[13] for an improved 5″/54 projectile. This projectile is 5.20 calibers in length, with a 2.75-caliber ogive nose, and 1-caliber conical boattail with 7.5-deg boattail angle. The theoretical calculations exhibited are based on a conical afterbody wake model and blunt nose with fuze geometry included. Exhibited in the figure is the C_{m_α} vs M_∞ variation from $M_\infty = 0.5$ to 2.0, demonstrating the capability of the method throughout and beyond the transonic regime. We note that the theoretical results agree very well for both overall trend and location of the peak pitching moment, with the magnitude of the predicted result being slightly higher throughout the entire range than the data indicate.

For this projectile, we performed several additional calculations to determine whether wind-tunnel interference effects were present in the data. Accordingly, we determined the TER equivalent body outer flow solution subject to both a solid and various porous wall boundary conditions. These calculations were performed at Mach numbers and in the vicinity of the C_{m_α} peak. All of these calculations resulted in indiscernible changes from the free air result provided in Fig. 14. We conclude that the discrepancy in C_{m_α} most likely is due to the midbody waisting on the actual projectile[13] that was not modeled in the theoretical calculations.

In the final figure we present results which demonstrate the capability of the present predictive method to treat a variety of different projectile boattail shapes, both axisymmetric and nonaxisymmetric. Figure 15 presents the predicted variation of C_{m_α} with M_∞ for the two nonaxisymmetric boattail shape projectiles shown previously in Fig. 4, plus two conical boattail projectiles and the corresponding cylindrical boattail projectile. All of these projectiles have a 5-caliber overall length and identical 2-caliber sharp ogive nose geometry. Consequently, the results presented illustrate, in a design sense, the effect on C_{m_α} of varying the boattail shape through a wide range of geometries. We note that the 1-caliber conical boattail projectile exhibits the highest C_{m_α} and thus is the worst choice from a stability design criterion. Decreasing the conical boattail length to 0.5 caliber improves the situation somewhat, but not significantly. The square boattail length further improves the situation, but the triangular boattail, of these four shapes, provides the best results for minimum peak C_{m_α}. These results are in direct correspondence with the experimental results of Ref. 1. Although the cylindrical boattail exhibits the lowest peak C_{m_α}, its high drag and consequent low range make it an undesirable candidate shape.

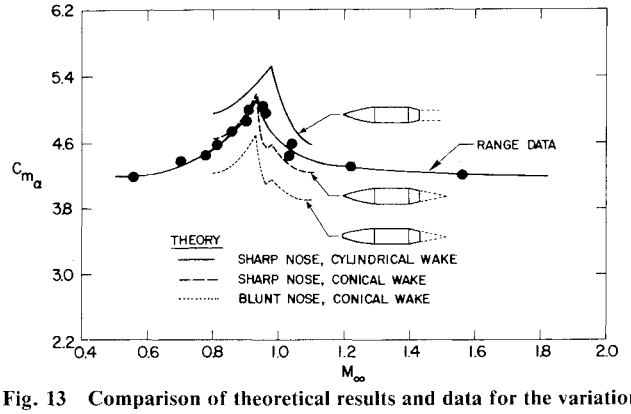

Fig. 13 Comparison of theoretical results and data for the variation of C_{m_α} vs M_∞ for a T388 projectile illustrating the effect of wake geometry and nose bluntness.

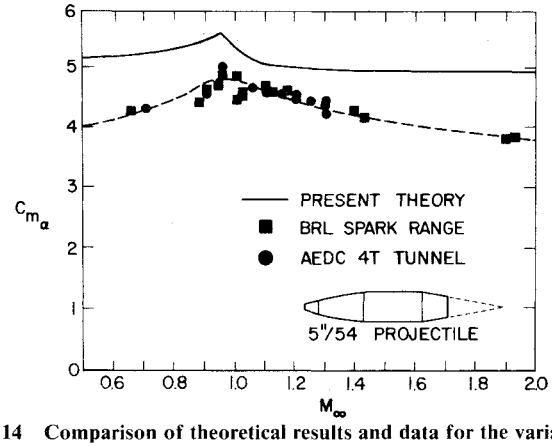

Fig. 14 Comparison of theoretical results and data for the variation of C_{m_α} vs M_∞ for the improved 5″/54 projectile.

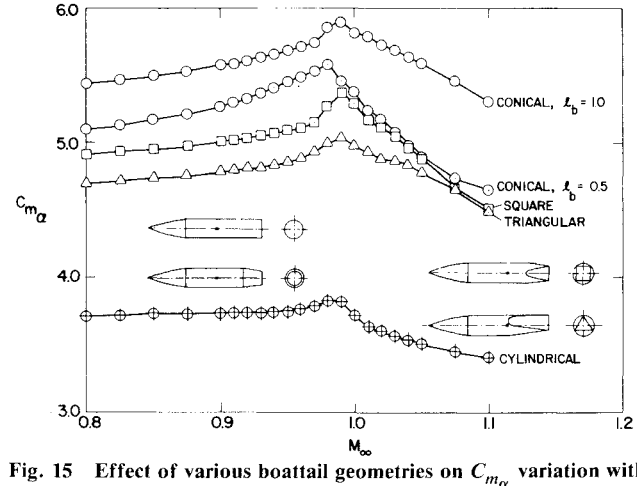

Fig. 15 Effect of various boattail geometries on C_{m_α} variation with M_∞ for a 5-caliber length, fixed nose geometry projectile.

Finally, we point out the computational efficiency of the present method. A complete calculation (TER computation plus loading determination) requires less than 30 sec CPU time on a CDC 7600 for a typical projectile at a specified M_∞. As a typical example, consider the theoretical predictions of C_{m_α} provided in Fig. 15 for the five different boattail projectiles. The separate points on each of the curves indicate the individual calculations and total 110 separate TER and loading determinations. Computational time for all of these cases was less than 30 min of CDC 7600 CPU time.

Concluding Remarks

The development of a theoretical predictive method for determining the steady inviscid aerodynamic behavior of ballistic projectiles throughout the transonic regime is described. The emphasis of the work was directed toward establishing the capability for investigating the now standard conical boattail projectiles as well as a variety of new shapes characteristic of the nonaxisymmetric boattail projectiles under current study by the U.S. Army.

The theoretical analysis is based on the transonic equivalence rule and includes a finite-difference procedure for determining the nonlinear axisymmetric outer (far field) flow about the equivalent body of revolution, and a two-dimensional finite element solver for providing general solutions to the inner (near field) cross flow problem for the arbitrary geometries characteristic of the new boattail projectiles. A nonlinear loading calculation procedure which incorporates transonic effects has been formulated and tested. The technique is based on apparent mass concepts and employs the finite element inner cross-flow solver to determine the appropriate apparent mass coefficients and uses the nonlinear outer TER solutions for the axisymmetric flow about the equivalent body to account for nonlinear effects due to shock waves.

Results are presented for a wide variety of projectile shapes, having both axisymmetric and nonaxisymmetric boattail geometries. They demonstrate the ability of the procedure to predict successfully the observed range and tunnel variations of destabilizing pitching moment throughout the transonic range. Additional calculations illustrating the separate effects of different geometry models to simulate the afterbody wake and nose bluntness, including fuze geometries, are presented.

Acknowledgments

This research was supported by the U.S. Army Research Office under Contract DAAG29-77-C-0038 with Dr. Robert Singleton as Technical Monitor.

References

[1]Platou, A. S., "Improved Projectile Boattail," *AIAA Journal,* Vol. 12, Dec. 1975, pp. 727-732.

[2]Stahara, S. S. and Spreiter, J. R., "Transonic Flows Past Nonaxisymmetric Slender Shapes—Classical Equivalence Rule Analysis," *AIAA Journal,* Vol. 17, March 1979, pp. 245-252.

[3]Stahara, S. S. and Spreiter, J. R., "Transonic Wind Tunnel Interference Assessment-Axisymmetric Flows," *AIAA Journal,* Vol. 18, Jan. 1980, pp. 63-71.

[4]Bryson, A. E. Jr., "Stability Derivatives for a Slender Missile with Application to a Wing-Body-Vertical Tail Configuration," *Journal of the Aeronautical Sciences,* Vol. 20, No. 5, 1953, pp. 297-308.

[5]Nielsen, J. N., *Missile Aerodynamics,* McGraw-Hill, New York, 1960.

[6]Heaslet, M. A. and Spreiter, J. R., "Three-Dimensional Transonic Flow Theory Applied to Slender Wings and Bodies," NACA Rept. 1318, 1957.

[7]Cheng, H. K. and Hafez, M. M., "Transonic Equivalence Rule: A Nonlinear Problem Involving Lift," *Journal of Fluid Mechanics,* Vol. 72, 1975, pp. 161-188.

[8]Klopfer, G. H. and Chaussee, D. S., "Numerical Solution of Three Dimensional Transonic Flows Around Axisymmetric Bodies at Angle of Attack," Nielsen Engineering & Research, Inc., TR 176, Feb. 1979.

[9]Spreiter, J. R. and Stahara, S. S., "Calculative Techniques for Transonic Flows About Certain Classes of Airfoils and Slender Bodies," NASA CR-1722, April 1971.

[10]Reklis, R. P., Danberg, J. E., and Ingu, G. R., "Boundary Layer Flows on Transonic Projectiles," AIAA Paper 79-1551, July 1979.

[11]Reklis, R. P., Sturek, W. B., and Bailey, R. R., "Computation of Transonic Flow Past Projectiles at Angle of Attack," AIAA Paper 78-1182, July 1978.

[12]Krial, K. S. and MacAllister, L. C., "Aerodynamic Properties of a Family of Shells of Similar Shape—105mm XM308E5, XM308E6, T388 and 155mm T387," Ballistics Research Lab. Memo Rept. 2023, Feb. 1970.

[13]Ohlmeyer, E. J., "Dynamic Stability of the Improved 5″/54 Projectile," NWL Tech. Rept. TR 2871, Dec. 1972.